

## Modulated wick heat pipe

G.S. Hwang<sup>a</sup>, M. Kaviany<sup>a,\*</sup>, W.G. Anderson<sup>b</sup>, J. Zuo<sup>b</sup>

<sup>a</sup> *Department of Mechanical Engineering, University of Michigan, Ann Arbor, MI 48109, United States*

<sup>b</sup> *Advanced Cooling Technologies, Inc., Lancaster, PA 17601, United States*

Received 15 May 2006; received in revised form 8 September 2006

Available online 17 November 2006

### Abstract

In heat pipes, modulation of evaporator wick thickness provides extra cross-sectional area for enhanced axial capillary liquid flow and extra evaporation surface area, with only a moderate increase in wick superheat (conduction resistance). This modulated wick (periodic stacks and grooves over a thin, uniform wick) is analyzed and optimized with a prescribed, empirical wick superheat limit. A thermal-hydraulic heat pipe figure of merit is developed and scaled with the uniform wick figure of merit to evaluate and optimize its enhancement. The optimal modulated wick for the circular and flat heat pipes is found in closed-form expressions for the viscous-flow regime (low permeability), while similar results are obtained numerically for the viscous-inertial flow regime (high permeability which is also gravity sensitive). The predictions are compared with the experimental result of a prototype (low permeability, titanium/water pipe with the optimal design) heat pipe which gives a scaled figure of merit of 2.2. Good agreement is found between the predicted and measured performance. The maximum enhancement is limited by the pipe inner radius (tapering of the stacks), the wick effective thermal conductivity, and the prescribed wick superheat limit.

© 2006 Elsevier Ltd. All rights reserved.

*Keywords:* Modulated wick; Optimal design; Figure of merit; Heat pipe; Critical heat flux; Superheat

### 1. Introduction

The modulation of heat pipe wick thickness assists axial capillary liquid flow, while limiting the increase in the wick superheat that accompany thicker, uniform wicks [1]. Fig. 1 shows the modulated wick structure with heat and liquid flow paths in the evaporator, evaporation surface (sites) and a prototype modulated wick heat pipe. The thick wick portion of the modulated wick (stacks) decreases the liquid flow resistance, and the thin wick portion (i.e., grooves) reduces the wick superheat. This modulation of the evaporator is used to design high performance heat pipes for microgravity applications [2,3]. The modulated wick has capillary arteries (with an azimuthally regular interval) connected to a thin, uniform wick lining the tube,

which feeds liquid to the evaporator. The liquid is vaporized on the entire surface of the modulated wick where the influx heat is exhausted, and moves back to the condenser as vapor phase to make a circulation loop. One method of fabrication uses rectangular-shaped mandrels to create grooves in a thick, uniform wick heat pipe. Due to the rectangular-shaped groove between adjacent stacks and the pipe curvature, each stack has a trapezoidal geometry. When the initial thick wick is deep, this results in a triangle shape, and the height of each stack has the maximum value limited by the base width of the stack. The modulated wick can also be extruded when the base width is below several particle diameters.

Fig. 2(a) and (b) show the enhancement of the critical heat flow rate for the prototype heat pipe tested in this paper. The prototype heat pipe has a  $R/\delta = 17.4$ , and titanium is used for pipe and working fluid is water. Fig. 2(a) shows the enhancement by the modulated wick heat pipe geometry up to the wick superheat limit. The enhancement

\* Corresponding author. Tel.: +1 734 936 0402; fax: +1 734 647 3170.  
E-mail address: [kaviany@umich.edu](mailto:kaviany@umich.edu) (M. Kaviany).

## Nomenclature

$A$	(cross-section) area ( $\text{m}^2$ )
$C_E$	Ergun coefficient
$c_p$	specific heat ( $\text{J/kg}$ )
$D^d$	dispersion coefficient ( $\text{m}^2/\text{s}$ )
$g$	gravitational acceleration ( $\text{m/s}^2$ )
$\Delta h_{\text{lg}}$	enthalpy of vaporization ( $\text{J/kg}$ )
$L$	length or height (m)
$L_s^*$	dimensionless height of stack
$K$	thermal conductivity ( $\text{W/m K}$ )
$K$	permeability ( $\text{m}^2$ )
$\dot{M}$	mass flow rate ( $\text{kg/s}$ )
$N$	number
$P$	pressure (Pa)
$Q$	heat transfer rate (W)
$Q_{\text{CHF}}^*$	dimensionless critical heat transfer rate ( $=Q_{\text{CHF}}/Q_{\text{CHF,u}}$ )
$R$	radius of pore or meniscus or bubble (m)
$R$	pipe radius (m) or thermal resistance ( $\text{W/K}$ )
$R^*$	dimensionless radius of pipe ( $=R/\delta$ )
$T$	temperature (K)
$U$	velocity (m/s)
$V$	specific volume ( $\text{m}^3/\text{kg}$ )
$W$	width (m)

### Greek symbols

$\alpha$	constant in thermal resistance model
$\delta$	wick thickness (m)

$\delta'$	equivalent wick thickness (m)
$\varphi$	angle (deg)
$\mu$	viscosity (Pa s)
$\rho$	density ( $\text{kg/m}^3$ )
$\sigma$	surface tension (N/m)

### Subscripts

a	adiabatic section
b	bubble
c	capillary or critical or condenser
CHF	critical heat flux
e	evaporator
f	flat heat pipe
g	gas or gap
k	conduction
l	liquid
lg	phase change, or saturation
n	discrete number, normal
p	pore
r	radial
s	surface or stack or solid particle
u	uniform wick
v	vapor
w	wick
$\perp$	lateral

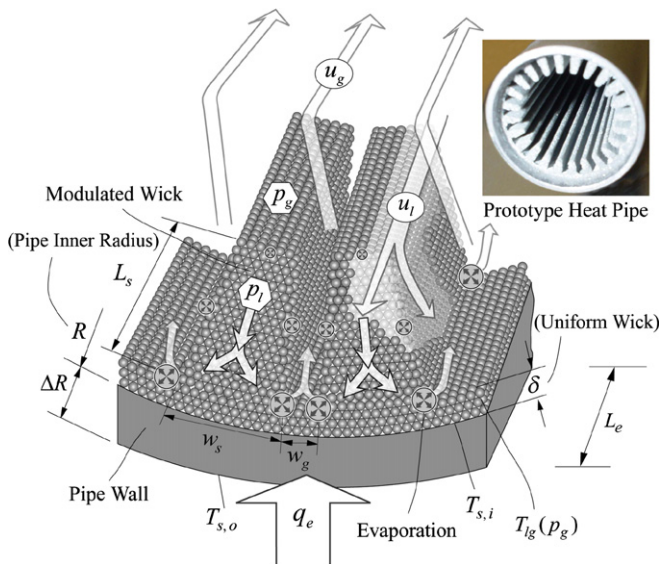


Fig. 1. Schematic of the modulated wick geometry in the evaporator, and the liquid/vapor flow paths and evaporation surface (sites). The photograph of the prototype modulated wick heat pipe is also shown.

of a flat heat (very large radius) pipe is also shown as an asymptotic upper limit. The critical heat flow rate (dryout

limit) for modulated wick heat pipe  $Q_{\text{CHF}}$  is scaled using that for non-modulated (i.e., thin, uniform) wick  $Q_{\text{CHF,u}}$ , while wick superheat is normalized by the maximum allowable (a prescribed value) wick superheat. The enhancement is attributed to a decrease in the liquid flow resistance by expanding cross-sectional area of the modulated wick until the axial liquid pressure drop reaches the capillary limit. The critical heat flow rate enhances as the pipe radius increases, since a tapered stack geometry (this is in part dictated by fabrication) becomes rectangular, reaching the flat heat pipe ( $R/\delta \rightarrow \infty$ ) limit. Hereafter,  $R^* = R/\delta$ . The maximum predicted enhancement of the prototype heat pipe (with a wick thermal conductivity  $\langle k \rangle = 4.4 \text{ W/m K}$ ) is  $Q_{\text{CHF}}/Q_{\text{CHF,u}} = 4.3$ , since the critical heat flow is also controlled by an effective thermal resistance. Fig. 2(b) shows further enhancement is possible with larger wick effective thermal conductivity. For the prototype (circular) heat pipe geometry, using titanium–water, the enhancement is  $Q_{\text{CHF}}/Q_{\text{CHF,u}} = 3.1$ , while it can increase up to  $Q_{\text{CHF}}/Q_{\text{CHF,u}} = 7$  by a copper–water combination. Hereafter,  $Q_{\text{CHF}}^* = Q_{\text{CHF}}/Q_{\text{CHF,u}}$ .

Here, we study the modulated heat pipe without curvature effect proposed in [1] to arrive at the optimal wick structure design. The pipe curvature affects the liquid flow cross-sectional area as well as the wick thermal resistance.

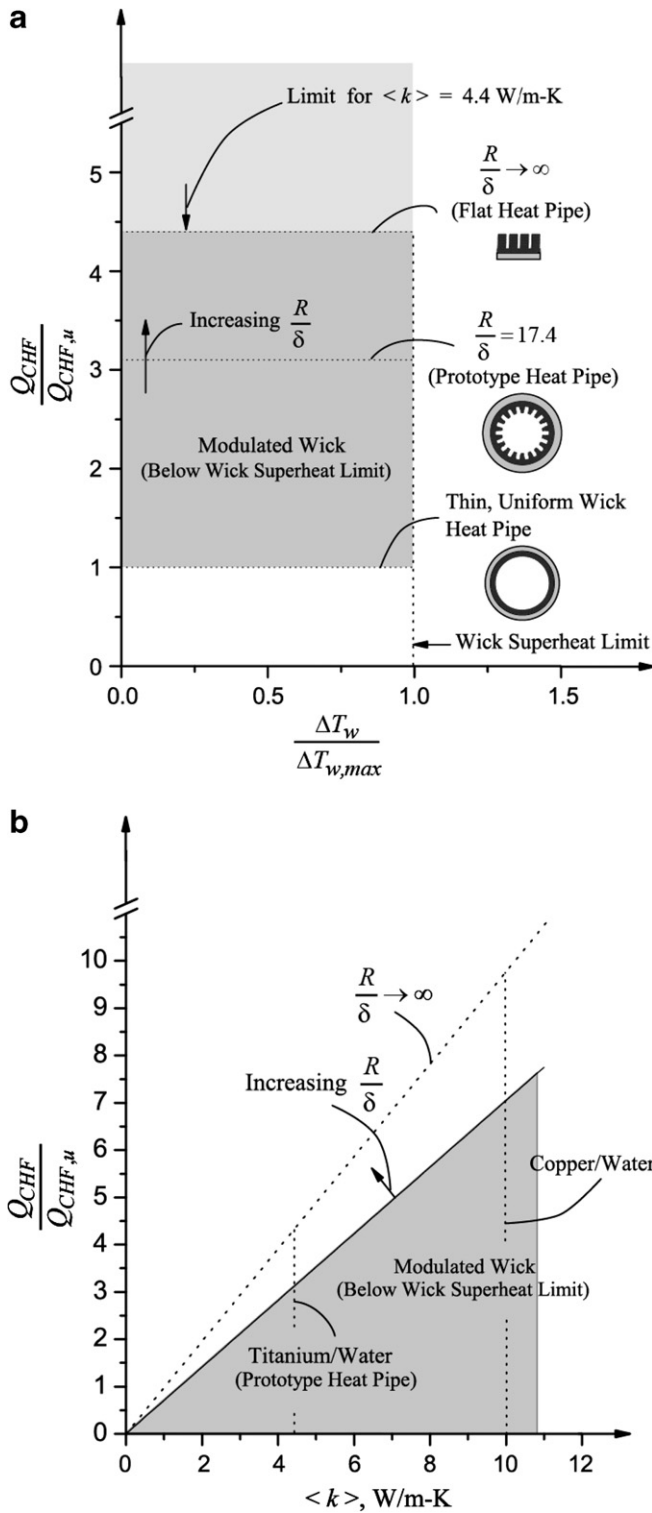


Fig. 2. The dimensionless (scaled using the thin, uniform wick) enhancement of the critical heat flow rate of the prototype heat pipe. The enhancement of the flat heat pipe is marked as an asymptotic, upper limit (based on imposed wick superheat limit). (a) Dimensionless critical heat flow rate enhancement for the prototype heat pipe, with respect to the wick superheat limit (for  $\langle k \rangle = 4.4 \text{ W/m K}$ ), and (b) same as (a), but with respect to the wick thermal conductivity  $\langle k \rangle$ . The titanium–water and copper–water heat pipes are marked. The enhancement of the flat heat pipe is also shown as an asymptotic, upper limit.

We use network models for the liquid flow and heat transfer in the evaporator, and in the case of low wick permeability obtain a closed-form solution for the heat pipe performance. We introduce a dimensionless heat pipe figure of merit to express the enhancement, and discuss its physics and the various limits in the viscous- and inertial-flow regimes. The case of flat heat pipe (no curvature effects) is also studied as the limit.

2. Theory

2.1. Liquid flow and heat transfer in modulated wick

In order to predict the steady-state heat pipe performance, the liquid flow and heat flow in the modulated wick must be modeled. Without a visual observation of the phenomena within the modulated wick, some simplifying assumptions are made with regard to the liquid flow paths in order to develop network models that predict the critical heat flow rate and wick superheat. Fig. 3 shows a proposed physical model for the liquid and heat flow paths of the modulated wick. This model is based on the geometry of the prototype heat pipe, and the wick is assumed to be a porous medium of uniform porosity and axially uniform (with lateral periodicity). Local volume-averaged liquid velocity and average thermal-hydraulic properties at the saturation temperature are assumed in order to simplify the analysis of liquid transport through the wick. It is assumed that complete phase change occurs over the modulated wick surface and vapor moves toward the condenser. The heat flows from the pipe wall towards the surface of the modulated wick to provide energy for phase change. The meniscus on the wick surface provides the curvature required for the capillary pumping for axial liquid flow. It is assumed that the axial liquid flow passes along the center of mass of the wick. As will be shown, even though the heat can flow up to the top of the stack, a large portion of it moves toward grooves where the thermal resistance is lowest. Based on the preceding assumptions,

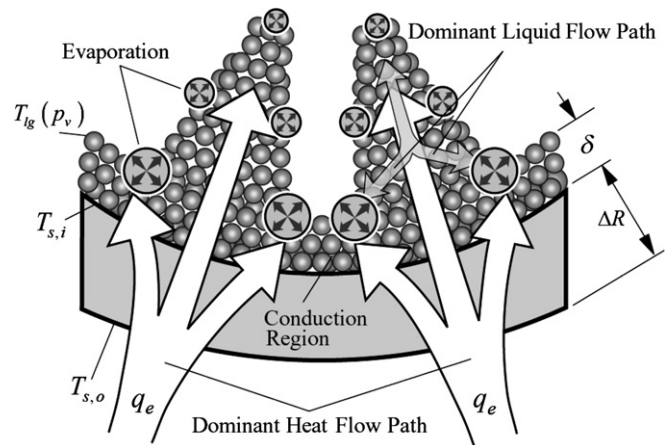


Fig. 3. Physical models for the heat and liquid flow paths and evaporation sites in the evaporator. The thin, uniform wick thickness  $\delta$ , is also shown.

the continuity, momentum, and energy conservation equations are written and solved. The vapor pressure everywhere in the evaporator is assumed to be uniform and corresponding to the saturation pressure. Assuming that evaporation occurs on the wick surface only and the fluid flow is incompressible, the continuity equation is

$$\nabla \cdot \mathbf{u}_l = 0 \quad \text{and} \quad \nabla \cdot \mathbf{u}_v = 0, \quad (1)$$

where  $\mathbf{u}_l$  and  $\mathbf{u}_v$  are the liquid and vapor velocity vectors. The area integral over the evaporation surface gives

$$\rho_l \int_A (\mathbf{u}_l \cdot \mathbf{s}_n) dA = \dot{M}_l, \quad (2)$$

where  $\dot{M}_l$  is the total liquid mass flow rate,  $A$  is the control surface area, and  $\mathbf{s}_n$  is the surface normal unit vector. The total mass flow rate determined by the total influx heat,  $Q$  and the heat of evaporation of liquid  $\Delta h_{lg}$ , can be written as

$$\dot{M}_l = \dot{M}_{lg} = \frac{Q}{\Delta h_{lg}} = \int_{A_{lg}} \dot{m}_{lg} dA_{lg}, \quad (3)$$

where  $\dot{m}_{lg}$  is the local surface evaporation rate per unit area and  $A_{lg}$  is the evaporation surface area. For the momentum in steady-state, Darcy–Ergun momentum relation [4] can be applied both in axial and radial liquid pressure drop

$$0 = -\nabla p_l + \rho_l g - \frac{\mu_l}{K} \langle \mathbf{u}_l \rangle - \frac{C_E}{K^{1/2}} \rho_l |\langle \mathbf{u}_l \rangle| \langle \mathbf{u}_l \rangle, \quad (4)$$

where  $p$  is the pressure,  $\langle \mathbf{u}_l \rangle$  is the volume-averaged liquid velocity vector through the stack,  $K$  is the wick permeability,  $C_E$  is the Ergun coefficient,  $\mu_l$  is the liquid viscosity,  $C_E = (0.018/\varepsilon^3)^{1/2}$ , and  $\varepsilon$  is the wick porosity. The frictional and the inertial pressure drop also determine the total liquid pressure drop along the axial direction of the pipe. Gravity is also included to control the pressure drop with respect to the angle placement of the heat pipe.

For low wick permeability ( $K \rightarrow 0$ ), the inertial term is not significant and also the gravity term becomes less important. As the wick permeability increases, both of these terms become significant, and the pipe orientation with respect to the gravity vector should be included. Here we concentrate on the low permeability wick and on the limited cases where consider the effect of permeability (or pore size), we consider only the horizontal arrangement of the pipe.

The total liquid pressure drop profile is limited by the capillary pumping capability,  $p_c$ , which allows for reaching the critical heat flow rate which is referred as viscous-drag liquid-dryout limit. The capillary pressure in the heat pipe with a porous medium is given as

$$p_c = 2\sigma \left( \frac{1}{r_{c,e}} - \frac{1}{r_{c,c}} \right), \quad (5)$$

where  $\sigma$  is the surface tension of the fluid, and  $r_{c,e}$  and  $r_{c,c}$  are the single principal capillary radii for the evaporator and condenser. Here, the  $r_{c,e}$  is set equal to the pore radius  $r_p$  of the evaporator, and the  $r_{c,c}$  is equal to half of the condenser groove width for the prototype heat pipe.

Thermal energy should also be conserved within the wick in the evaporator. Under steady-state condition with surface evaporation only, the local thermal energy equation is simplified as [5]

$$\nabla \cdot \mathbf{q} = 0. \quad (6)$$

The integral over the evaporator surface gives

$$Q = \int_A (\mathbf{q} \cdot \mathbf{s}_n) dA = \dot{M}_{lg} \Delta h_{lg}, \quad (7)$$

where  $Q$  is the heat flow rate into the evaporator and  $A_e$  is the evaporation surface area. The radial liquid flow moving toward the grooves of the modulated wick would be a counter-flow of the heat, but the low radial liquid velocity and the short height of the stack lead to the low Péclet number in the radial (lateral) direction,  $Pe_\perp$  [where  $Pe_\perp = (\rho c_p)_l \langle u_\perp \rangle_1 L_s / \langle k \rangle$ ] indicating the radial (lateral) heat conduction is dominant over the opposing convection heat transfer process within the wick. The radial heat conduction equation transfer formulates with dispersion in porous media as well as the wick thermal conductivity in the following equation:

$$\mathbf{q}_k = -[\langle k \rangle + D_\perp^d (\rho c_p)_l] \nabla T, \quad (8)$$

where  $D_\perp^d$  is the radial (lateral) thermal dispersion in the wick. Assuming that the wick is made of spheres it can be written as [4]

$$D_\perp^d = Pe_\perp \frac{3k_l}{16(\rho c_p)_l}. \quad (9)$$

Thermal dispersion in the wick is negligibly small due to both the low  $Pe_\perp$  and relatively high liquid density. Thus, Eq. (8) becomes a basic heat conduction equation

$$\mathbf{q}_k = -\langle k \rangle \nabla T. \quad (10)$$

Even though the modulated wick produces 2-D liquid and heat flow paths, a valid simplification of 1-D models is given in the following section.

## 2.2. Liquid flow network model

Liquid flow through the modulated wick is modeled assuming that (1) a porous medium is uniform, isotropic, and fully saturated with liquid, (2) liquid properties are evaluated by the saturation temperature, (3) liquid velocity is uniform within the wick, (4) stack unit cell is symmetric by the center of the stacks, (5) liquid flow passes through the centroid of the stack, (6) peripheral (radial) gravity effect on liquid flow is negligible, (7) heat flux and local mass flow rate in the evaporator are uniform.

Fig. 4 shows the axial and radial liquid flow resistances for the modulated wick, and local liquid pressure and mass flow rate in a discretized domain. The liquid flow network model is developed in viscous and inertial flow regimes, which is influenced by the pore size (permeability and maximum capillary pressure) of the wick, and the heat flow rate.

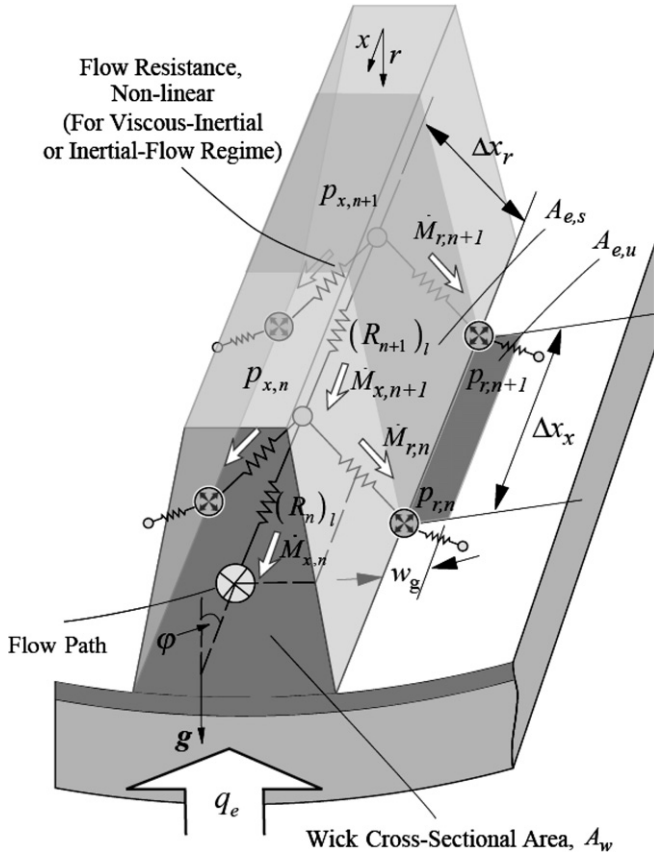


Fig. 4. Liquid flow network model, for the radial-axial flow and the thermal network model. The evaporation surface is also shown. The liquid flow resistance is non-linear for the liquid velocity in the viscous-inertial flow regime.

### 2.2.1. Viscous-flow regime

In a viscous-flow regime (fine porous medium and small permeability,  $K \rightarrow 0$ ) and no gravity condition, the liquid pressure drop in the evaporator (axial direction only) is simplified taking the evaporator length integral of Eq. (4) as

$$\Delta p_{1,L_c} = \frac{\mu_1}{K} \langle u_1 \rangle_{L_c} L_c, \quad (11)$$

where  $\Delta p_{1,c}$  is the liquid pressure drop in the evaporator,  $\mu_1$  the liquid viscosity,  $L_c$  is the evaporator length, and  $\langle u_1 \rangle_{L_c}$  is the averaged liquid velocity along the evaporator, i.e.,

$$\langle u_1 \rangle_{L_c} = \frac{1}{L_c} \int_0^{L_c} u_1(x) dx, \quad (12)$$

and then, the radial liquid pressure drop is neglected due to small liquid velocity within the wick. The simple form of the liquid pressure drop allows for a closed-form solution of the critical heat flow rate which will be discussed following section.

### 2.2.2. Viscous- and inertial-flow regimes

In viscous- and inertial-flow regimes (coarse pores, i.e. large permeability), the liquid pressure drop in the evaporator is given as

$$\Delta p_{1,x} = \left( \frac{\mu_1}{K} \langle u_1 \rangle_{L_c} + \frac{C_E}{K^{1/2}} \rho_1 \langle u_1 \rangle_{L_c}^2 - \rho_1 g \cos \varphi \right) L_c, \quad (13)$$

where  $\varphi$  is the angle that the heat pipe makes with respect to the horizontal line. Note that  $\varphi = \pi/2$  indicates the pipe is horizontally placed, and  $\varphi = 0$  presents the evaporator is directly below the condenser (gravity aided).  $\varphi = \pi$  shows that the condenser is below the evaporator (gravity hindered). Similarly, the radial liquid pressure drop within the wick is also given as

$$\Delta p_{1,r} = \left( \frac{\mu_1}{K} \langle u_1 \rangle_r + \frac{C_E}{K^{1/2}} \rho_1 \langle u_1 \rangle_r^2 \right) \Delta x_r, \quad (14)$$

where  $\langle u_1 \rangle_r$  is the radial liquid velocity within the wick, and  $\Delta x_r$  is the radial distance of the liquid flow within the stack. The gravity is negligible due to small  $\Delta x_r$  compared to  $L_c$ . Numerical calculations are required to determine these two pressure drops since they are also influenced by the local mass flow rate. The uniform evaporation rate on every modulated wick surface is assumed

$$2\dot{M}_{r,n} = \frac{Q_n}{N_s \Delta h_{lg}}, \quad (15)$$

where  $\dot{M}_{r,n}$  is the local liquid mass flow rate toward one side of the stack at each node, and  $Q_n$  is the heat flow rate at each node along the circumference of the pipe. To obtain the heat flow rate both at each node and stack,  $Q_n$  is divided by the number of stacks  $N_s$ . For the axial flow, the continuity can be modeled as

$$\dot{M}_{x,n} = \dot{M}_{x,n+1} - 2\dot{M}_{r,n}. \quad (16)$$

The downstream axial liquid flow rate  $\dot{M}_{x,n}$  should be conserved with the upstream axial flow rate  $\dot{M}_{x,n}$ , and the evaporation rate  $2\dot{M}_{r,n}$ . From Eqs. (13) and (14), the discretized momentum equations for the liquid pressure drop are established as

$$p_{x,n} = p_{x,n+1} - \left( \frac{\mu_1}{K} \langle u_{1,x,n} \rangle + \frac{C_E}{K^{1/2}} \rho_1 \langle u_{1,x,n} \rangle^2 \right) \Delta x_x + \rho_1 g \cos \varphi \Delta x_x, \quad (17)$$

$$\langle u_{1,x,n} \rangle = \dot{M}_{x,n} / \rho_1 A_w,$$

$$p_{r,n} = p_{x,n} - \left( \frac{\mu_1}{K} \langle u_{1,r,n} \rangle + \frac{C_E}{K^{1/2}} \rho_1 \langle u_{1,r,n} \rangle^2 \right) \Delta x_r, \quad (18)$$

$$\langle u_{1,r,n} \rangle = 2\dot{M}_{r,n} / \rho_1 (A_{e,s} + 2A_{e,u}),$$

where  $A_w$  is the cross-sectional area of the modulated wick,  $A_{e,s}$  is the evaporation surface area of the modulated wick, and  $A_{e,u}$  is the evaporation surface area for grooves (half bottom area of each groove as shown in Fig. 4).

### 2.3. Heat transfer (thermal resistance) network model

The assumptions for the heat transfer model are (1) uniform vapor/wick temperature at the interface between the wick and the vapor space, (2) steady-state heat transfer, (3) negligible temperature drop at the wick/vapor interface,

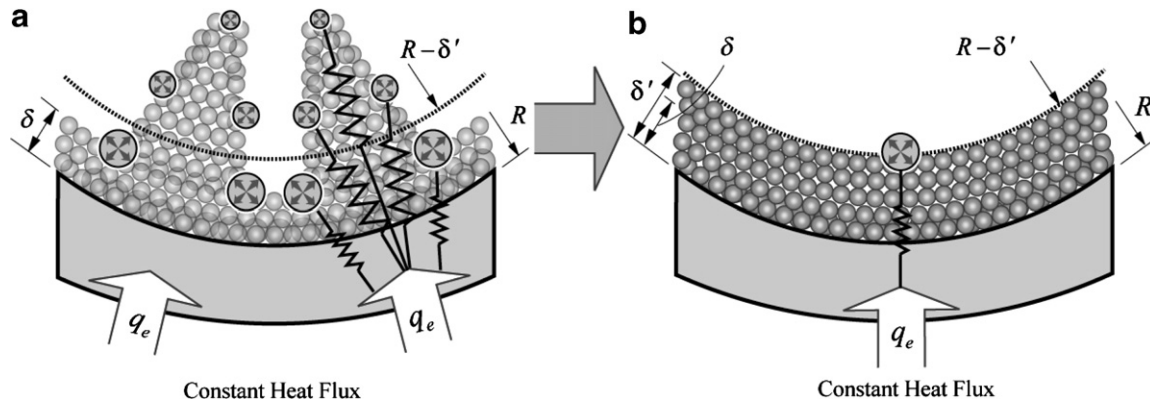


Fig. 5. The one-dimensional radial heat flow network model using equivalent wick thickness (modulated wick is presented as a thicker, uniform wick). (a) Modulated wick with various heat flow paths towards evaporation surface, and (b) equivalent uniform wick thickness  $\delta'$  with uniform thermal resistance.

- (4) negligible contact resistance at the wall/wick interface,  
 (5) uniform pipe (outer) wall heat flux.

Wick superheat  $\Delta T_w$  is defined as

$$\Delta T_w = T_{s,i} - T_{lg}, \quad (19)$$

where  $T_{s,i}$  represents the average temperature at the inner pipe surface (since uniform heat flux is prescribed at the outer surface), and the wick superheat is proportional to the wick thermal resistance. The surface temperature of the modulated wick (where the evaporation occurs) is set to the saturation temperature  $T_{lg}$ . For the modulated wick, an equivalent wick thickness  $\delta'$  is used as shown in Fig. 5. This equivalent 1-D conduction heat transfer model uses  $\delta'$  for an equivalent, uniform thermal resistance. Then we have

$$\Delta T_w = QR_k, \quad \text{and} \quad R_k = \frac{\Delta T_w}{Q} = \frac{\ln(1 - R^{*-1}\delta'^*)^{-1}}{2\pi\langle k \rangle L_c}, \quad (20)$$

where  $R^*$  is the dimensionless inner radius of the heat pipe, and  $\delta'^*$  is the dimensionless equivalent wick thickness. For  $\delta'^* = 1$ , the wick is uniform. It is found that the  $\delta'$  is a linearly proportional to the stack width  $w_s$ , i.e.,

$$\delta' - \delta = \alpha w_s, \quad (21)$$

where  $\alpha$  is the wick superheat constant which will be discussed in Appendix A.

### 3. Figure of merit and optimization

We optimize the modulated wick geometry for maximum performance which is stated as an increase in the critical heat flow rate  $Q_{CHF}$  with minimum increase in the wick superheat,  $T_{s,i} - T_{lg}$  (which is proportional to the wick thermal resistance, for a given effective wick conductivity  $\langle k \rangle$ ). The critical heat transfer rate of the modulated wick heat pipe is limited by the capillary pumping capability balanced by the viscous-inertial-gravity forces. Fig. 6(a) and (b) show a rendering of the heat pipe with two different stack numbers. Fig. 6(a) shows large cross-sectional area of the axial artery wick (i.e., small groove area) enhances

the critical heat transfer rate, while it results in high wick superheat (due to longer conduction heat flow path). On the other hand, Fig. 6(b) illustrates a large number stacks leads to smaller conduction path (smaller wick superheat), but a loss of liquid flow area (reducing the critical heat transfer rate). Thus, the optimum modulated wick would have large artery cross-sectional area to minimize the liquid flow resistance, and also have enough number of grooves to maintain a moderate thermal resistance. These optimizations are similar to that of the previous published work [6]. To perform this optimization, the dimensionless modulated wick pitch (dimensionless stack width),  $w_s^*$  is chosen as the optimal design parameter (to determine the optimal pitch of stacks with given geometric constraints), i.e.,

$$w_s^* = \frac{w_s}{w_s + w_g} \quad \text{or} \quad w_s = \frac{w_s^* w_g}{1 - w_s^*}, \quad (22)$$

where  $w_s$ ,  $w_g$  is the base land width of the stack and groove, respectively.  $w_s^*$  is the portion of unit cell width covered by stack, and is related to the number of stacks

$$w_s^* = 1 - \frac{w_g N_s}{2\pi(R - \delta)} \quad \text{or} \quad N_s = \frac{2\pi(R - \delta)(1 - w_s^*)}{w_g}. \quad (23)$$

To investigate the heat pipe characteristics and optimization, a heat pipe figure of merit is established from the previous figure of merit [7]. The heat pipe figure of merit,  $Q_{CHF}/R_k$  is defined as the critical heat transfer rate divided by thermal resistance to evaluate overall heat pipe performance. For a uniform wick, the  $Q_{CHF}/R_k$  becomes 1. Assuming that the vapor pressure drop is neglected, the critical heat transfer rate of heat pipe by the phase change of liquid flow is given as

$$Q_{CHF,lg} = 2\langle u_1 \rangle_{L_c} A_w \rho_1 \Delta h_{lg}, \quad (24)$$

where  $A_w$  is a modulated wick cross-sectional area, namely  $A_w = A_{w,s} + A_{w,u}$ . The  $Q_{CHF}$  is finalized when the capillary pumping capability and the liquid pressure drop along the evaporator are considered in addition to the phase change configuration by Eq. (24)

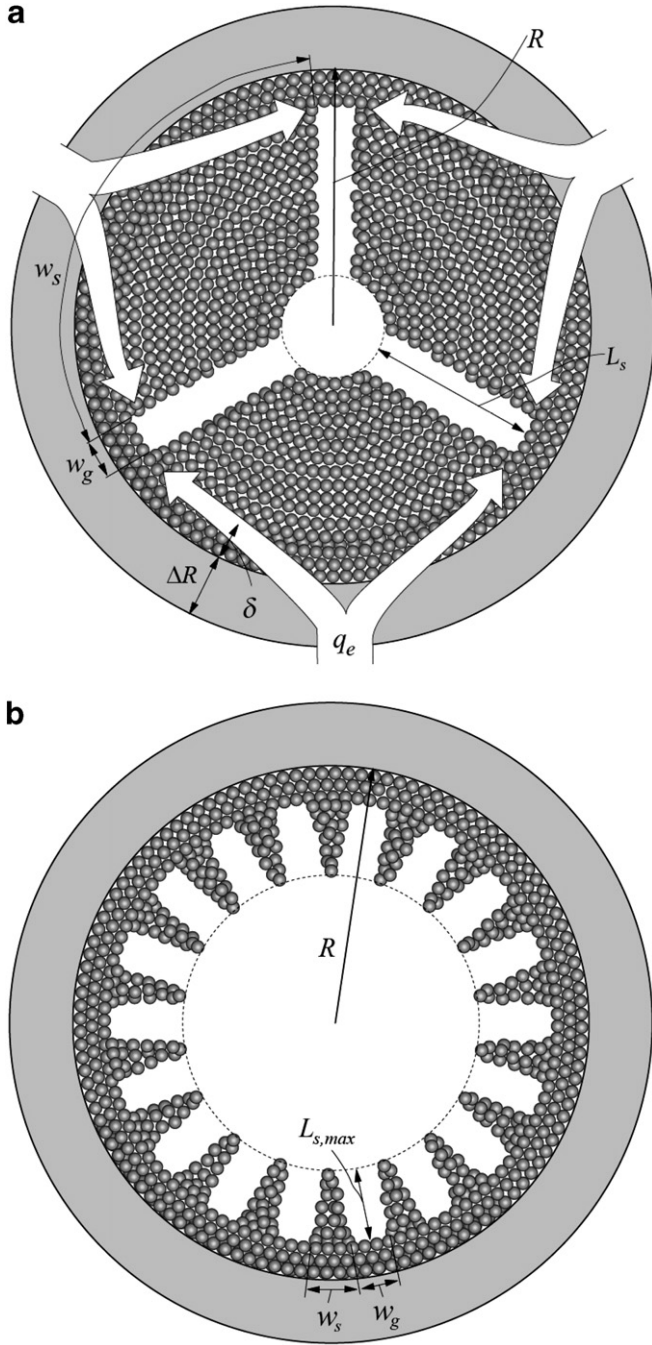


Fig. 6. Cross-sectional area of heat pipe showing the number of stacks  $N_s$ , with the maximum stack height  $L_{s,max}$  (imposed by the pipe radius and fabrication) marked. (a)  $N_s = 3$  with heat flow paths, and (b)  $N_s = 18$ .

$$Q_{CHF} = 2 \frac{p'_c}{\Delta p_{1,Lc}} \langle u_1 \rangle_{Lc} A_w \rho_l \Delta h_{lg}, \quad (25)$$

where  $p'_c$  is the effective capillary pressure. Thus, from Eqs. (20) and (25), the dimensional heat pipe figure of merit is defined as

$$\frac{Q_{CHF}}{R_k} = \frac{4\pi p'_c \langle u_1 \rangle_{Lc} A_w \rho_l \Delta h_{lg}}{\Delta p_{1,Lc}} \frac{\langle k \rangle}{\ln(R/R - \delta')}. \quad (26)$$

In general, the effective capillary pumping capability is reduced by the liquid pressure drops in the condenser and in the adiabatic section. Then, the effective capillary pressure in the evaporator is

$$p'_c = p_c - \Delta p_{1,a} - \Delta p_{1,c}, \quad (27)$$

where  $\Delta p_{1,a}$  is the liquid pressure drop in the adiabatic section, and  $\Delta p_{1,c}$  is the liquid pressure drop in the condenser. The various liquid pressure drops are also estimated using the Darcy–Ergun momentum equation, Eq. (4). The uniform wick of the adiabatic section and the rectangular-groove wick of the condenser section are made of sintered particles, in the prototype heat pipe.

In the viscous-flow regime, the dimensional heat pipe figure of merit is obtained by Eqs. (11) and (26), and then is simplified as

$$\frac{Q_{CHF}}{R_k} = \frac{4\pi p'_c K A_w \rho_l \Delta h_{lg}}{\mu_l} \frac{\langle k \rangle}{\ln(R/R - \delta')} \quad (28)$$

modulated wick figure of merit for low permeability.

Note that the figure of merit contains the key thermo-physical and geometric parameters, i.e., through the capillary pressure the surface tension and the pore radius, and also explicitly appearing are the permeability, wick cross-sectional area, liquid density, heat of evaporation, liquid viscosity, wick effective conductivity, pipe radius, and effective wick thickness.

The uniform wick heat pipe and the modulated wick heat pipe have different  $A_w$  and  $\delta'$ , while the other thermal-hydraulic parameters remain the same. In the uniform wick,  $A_w$  becomes  $A_{w,u}$  and  $\delta'$  is the same as  $\delta$ , and the modulated wick allows for  $A_w = A_{w,s} + A_{w,u}$ . To evaluate the enhancement of modulated wick heat pipes, the dimensionless heat pipe figure of merit scaled by the uniform wick heat pipe figure of merit is obtained as

$$\frac{Q_{CHF}^*}{R_k^*} = \left(1 + \frac{A_{w,s}}{A_{w,u}}\right) \frac{\ln(1 - R^{*-1})^{-1}}{\ln(1 - R^{*-1} \delta'^*)^{-1}} \quad (29)$$

scaled modulated wick figure of merit  
for low permeability,

where  $A_{w,u} = \pi[R^2 - (R - \delta)^2]$ ,  $A_{w,s} = \pi[R^2 - (R - L_s)^2] - N_s w_g L_s$ .

The flat heat pipe is also considered as  $R^* \rightarrow \infty$ . As the radius increases, the pipe appears to be planar wall and the stacks become rectangular as shown in Fig. 7, while the other geometric parameters remain same. Similarly, applying heat conduction equation in the planar wall, the dimensionless heat pipe figure of merit is given as

$$\frac{Q_{CHF}^*}{R_k^*} = \delta'^{* - 1} \left(1 + \frac{A_{w,s,f}}{A_{w,u,f}}\right), \quad (30)$$

where  $A_{w,u,f} = \delta(w_s + w_g)$ ,  $A_{w,s,f} = L_s w_s$ , and  $\delta'^* = 1$  for the uniform wick. At given  $L_s^*$ . The flat heat pipe provides the best performance and its enhancement is set to the upper

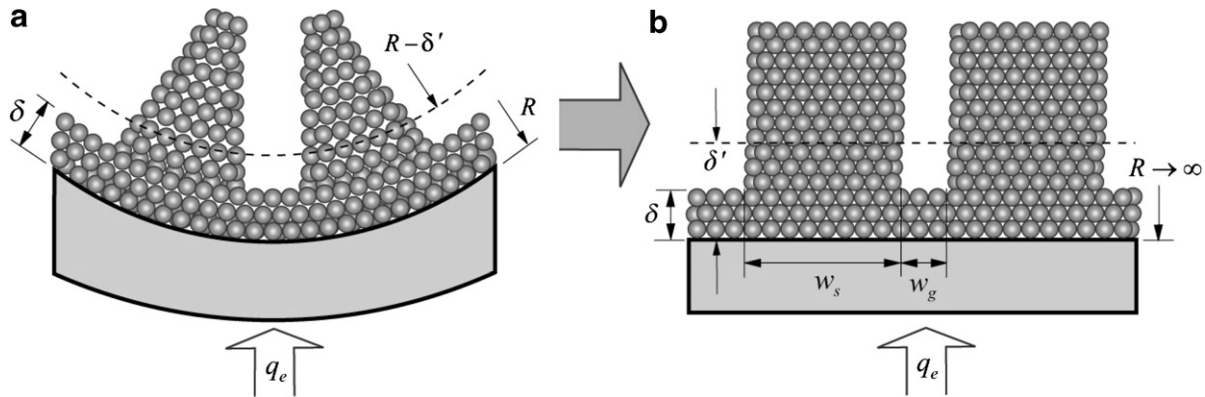


Fig. 7. Schematic of cross-sectional geometry of the prototype heat pipe: (a) evaporator, (b) adiabatic section, and (c) condenser.

limit. Finally, the dimensionless heat pipe figure of merit becomes

$$\frac{Q_{CHF}^*}{R_k^*} = \left[ 1 + \frac{L_s w_s}{\delta(w_s + w_g)} \right] \frac{\delta}{\delta + \alpha w_s} = \left\{ 1 + \frac{L_s \left( \frac{w_s^* w_g}{1 - w_s^*} \right)}{\left[ \frac{w_s^* w_g}{1 - w_s^*} \right] + w_g} \right\} \frac{1}{1 + \frac{\alpha}{\delta} \left( \frac{w_s^* w_g}{1 - w_s^*} \right)}$$

scaled modulate wick figure of merit for low permeability. (31)

As discussed, in the inertial-flow regime, the dimensionless heat pipe figure of merit is numerically obtained due to complexity of calculations. An inertial-flow pressure drop is also considered for a thin, uniform wick to evaluate the enhancement.

In the dimensional heat pipe figure of merit, Eq. (26), the performance increases as the permeability  $K$  increases (note that the maximum capillary pressure decreases as the permeability increases). However, the gravity dependence (orientation of the heat pipe) also becomes significant as the permeability  $K$  increases (e.g., the liquid flowing upward against the gravitational force). Here we will not address the gravity effect, assuming the pipe is located horizontally and also neglecting the radial variation of hydrostatic pressure.

#### 4. Experiment

The wick of the prototype heat pipe was fabricated with spherical CP-Ti (Commercially Pure Titanium) powder. To increase the heat pipe performance, the wicks in the evaporator, adiabatic section, and condenser have different designs for each section. The cross-sections of the prototype heat pipe are shown in Fig. 8, and the specifications are summarized in Tables 1 and 2. The heat pipe has a 25.4 mm OD, and 61 cm long. The 1.25 mm wall thickness is designed to endure the high pressure ( $\approx 2.7$  MPa) inside while operating at temperatures up to 260 °C. In the evaporator, the wick is fabricated using a  $-100$  mesh powder. In the modulated wick of the evaporator, the experimentally measured pore size is 18.4  $\mu\text{m}$ . The sintered powder forms both the thin, uniform layer coating,  $\delta$  as well as the artery wick  $L_s$ . The thin, uniform wick is 0.7 mm thick, with a groove width of 1.14 mm. The sintered titanium wick has a thermal conductivity of 4.4 W/m K. For ease of fabrication, the grooved condenser wick was fabricated using a  $-200$  mesh titanium powder. During heat pipe operation, liquid travels in the condenser grooves, as well as in the sintered lands. It can be shown that the fraction of liquid traveling in the sintered condenser lands is negligible, so there is no advantage to using a  $-100$  mesh wick in the condenser. The advantage of a  $-200$  mesh condenser

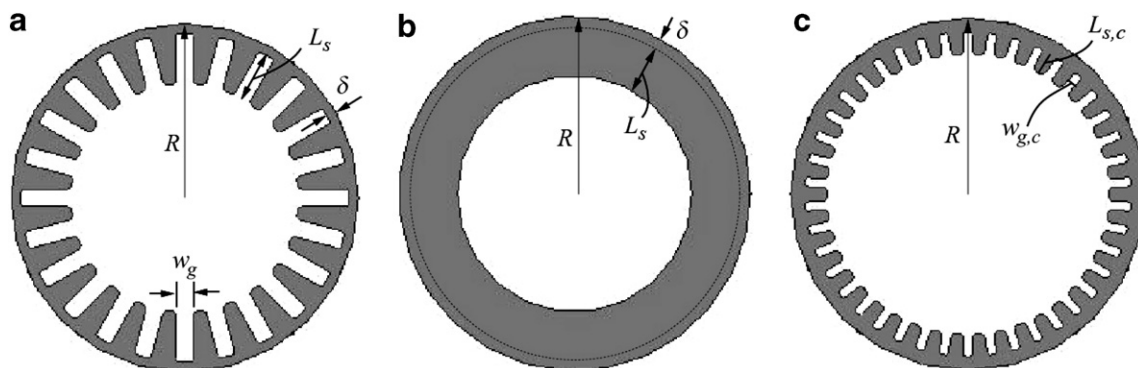


Fig. 8. Schematic of the experimental apparatus. Segmented heater is built on the evaporator, and the gas gap calorimeter on the condenser removing applied heat power at a constant temperature. The thermocouple locations are also shown.

Table 1  
Geometric parameters, thermophysical properties, and operating conditions for the prototype heat pipe [2,3]

Parameter	Magnitude	Parameter	Magnitude
$r_p$	18.4 $\mu\text{m}$	$N_c$	42
$k_l$	0.6 W/m K	$R$	11.45 mm
$k_s$	22 W/m K	$\Delta R$	1.25 mm
$\langle k \rangle$	4.4 W/m K	$T_{lg}(p_v)$	473 K
$K$	$5.68 \times 10^{-12} \text{ m}^2$	$w_g$	1.1 mm
$L_a$	0.025 m	$w_{g,c}^*$	0.58 mm
$L_c$	0.406 m	$w_s^*$	0.57 ( $N_s = 24$ )
$L_e$	0.152 m	$\varepsilon$	0.4
$L_s$	3.3 mm	$\delta$	0.7 mm
$L_{s,c}$	1.52 mm		

Table 2  
Titanium wick properties

Material	Powder	Pore size, $\mu\text{m}$	Permeability, $\text{m}^2$
CP titanium	–100	18.4	$5.68 \times 10^{-12}$
CP titanium	–200	15.5	$1.5 \times 10^{-12}$

wick is that there is a greater amount of shrinkage during fabrication, so that the mandrel is easier to remove. The adiabatic section is 25.4 mm long, and is composed of both powders. The half close to the evaporator is –100 powder, and the half close to the condenser is –200 powder. The height of the adiabatic wick is same as that of the modulated wick of the evaporator.

Fig. 9 shows the prototype heat pipe test station. A series of heater blocks and a gas gap calorimeter were used to test the modulated heat pipe at various heat fluxes and temperatures. Using the gas gap calorimeter, the temperature of a heat pipe can be kept constant while changing the power through the condenser. This is done by flowing different concentrations of argon and helium (with different thermal conductivities) in a gap between a jacket of cooling water and the condenser. The gas flow rate is very low, so that convection into the gas is negligible, and conduction through the gas gap dominates the thermal resistance. For instance, if it were desirable to increase the power while keeping the temperature of the pipe constant, the

flow rate of the higher conductivity gas (helium) would be turned up relative to the less conductive gas.

To measure the critical heat transfer rate, the adverse elevation of the heat pipe evaporator over the condenser is first fixed. The power is then slowly raised until the desired heat pipe evaporator temperature is reached. The heater input power, thermocouple temperatures, and cooling water flow rate are measured. The power is then increased slightly. The gas gap calorimeter helium/argon ratio is then adjusted to maintain the heat pipe evaporator temperature at the desired point. The temperatures, heater power, and water flow rate are measured once steady-state is reached. The critical heat transfer rate occurs when the evaporator starts to dryout, which causes the evaporator temperatures in the heat pipe to become non-uniform.

## 5. Results and discussion

### 5.1. Wick superheat limit

When the input heat is increased beyond the dryout threshold, nucleate boiling may occur in the wick structure and bubbles may become trapped in the wick. The vapor increases the resistance to the liquid flow (through the relative permeability which is a highly nonlinear function of the fraction of space occupied by the vapor). This results in premature evaporator dryout at the evaporation sites. The bubbles also cause an increase in the wick thermal resistance (due to decrease in the effective thermal conductivity) which in turn results in a significant increase in the wick superheat. This phenomenon, referred to as a wick superheat limit, is of critical consideration, and here it is designated by an empirical wick superheat limit which can reach the critical heat flow rate  $Q_{CHF}$  before a viscous-drag liquid-dryout limit. Ideally, boiling begins to occur when the pressure difference between the heat pipe inner surface,  $p_{s,i}$  and the vapor space,  $p_v$  is greater than the difference between a bubble and the maximum capillary pressure. The relation is given as [8,10,11]

$$P_{s,i} - P_v \geq 2\sigma \left( \frac{1}{r_b} - \frac{1}{r_{c,e}} \right), \quad (32)$$

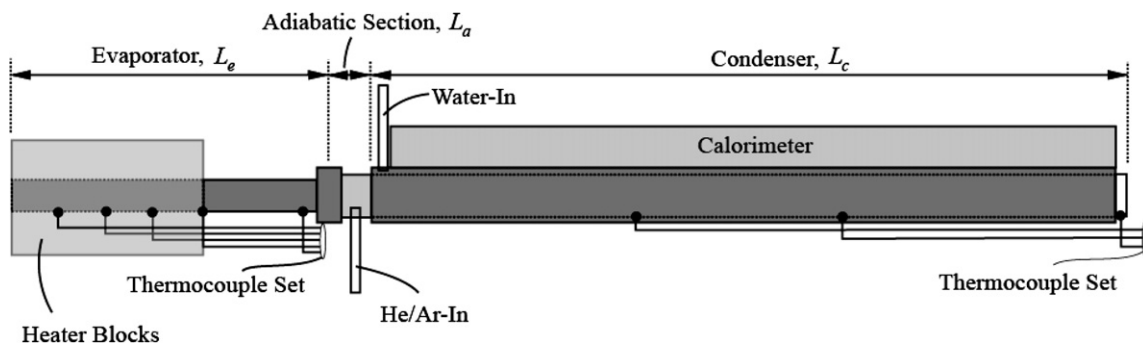


Fig. 9. Schematic of the circular and flat heat pipes, for the same wick pitch and height. The equivalent uniform wick thickness  $\delta'$  is also marked: (a) circular heat pipe, and (b) flat heat pipe. For the flat heat pipe,  $R^* \rightarrow \infty$ .

where  $r_b$  is the bubble radius. Assuming that the vapor adjacent to a meniscus is at saturation state, and applying the Clausius–Clapeyron equation between  $(p_v, T_v (\approx T_{lg}))$  and  $(p_{s,i}, T_{s,i})$ , this prescribed wick superheat is given as

$$\Delta T_w = T_{s,i} - T_{lg} \leq \frac{2\sigma T_v}{\Delta h_g \rho_v} \left( \frac{1}{r_b} - \frac{1}{r_{c,e}} \right). \quad (33)$$

The bubble radius can be predicted by

$$r_b = \left[ \frac{2\sigma T_v k_l (v_v - v_l)}{q \Delta h_g} \right], \quad (34)$$

where  $q$  is the heat flux,  $k_l$  is the liquid thermal conductivity, and  $v_v$  and  $v_l$  are the specific volume of saturated vapor and liquid, respectively. The predicted wick superheat limit shows it is less than 1 °C. This significantly under-predicts the measured effective wick superheat limit which is larger than, 10 °C suggested by the experimental results of [9]. Here we use a wick superheat limit (maximum allowable wick superheat) of 10 °C.

### 5.2. Pore radius and flow regimes

The wick pore radius (meniscus radius), is a key parameter controlling both capillary pumping capability and permeability which in turn influence the  $Q_{CHF}$ . Fig. 10 shows the predicted  $Q_{CHF}$  for the thin, uniform wick and the prototype heat pipe with respect to various pore radii at gravity-free environment. The  $Q_{CHF}$  in the inertial-flow regime is also compared with that for the viscous-flow regime which is predicted by closed-form solution. The empirical

correlation between pore size and permeability ( $K = 0.125r_p^{2.2}$ ) is used [2]. The variation of  $Q_{CHF}$  shows a linearly enhanced critical heat flow rate for small pore radii (<50 μm), where the viscous-flow (low liquid velocity) is dominant. Between 50 and 350 μm, the inertial-flow becomes progressively significant, and then the liquid flow resistance increases nonlinearly (viscous-inertial flow regime). Finally, the rate of the  $Q_{CHF}$  enhancement decreases as the pore radius becomes large, and then

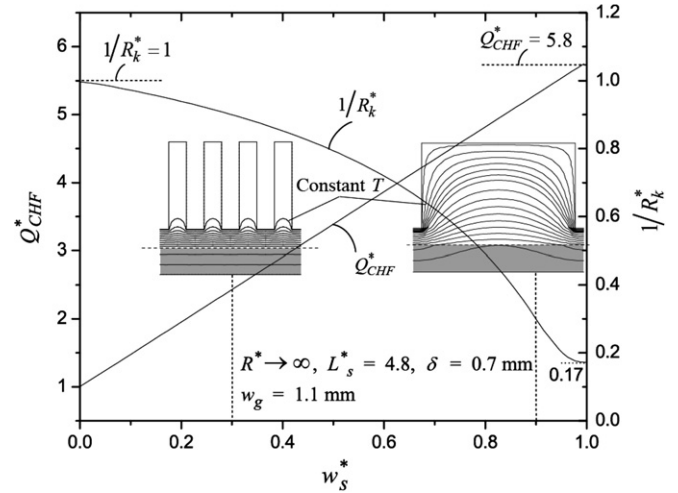


Fig. 11. Variation of the dimensionless critical heat flow rate  $Q_{CHF}^*$  and thermal resistance  $1/R_k^*$  with respect to the dimensionless modulated wick pitch  $w_s^*$  in the flat heat pipe, and the isothermal plot within the wick.

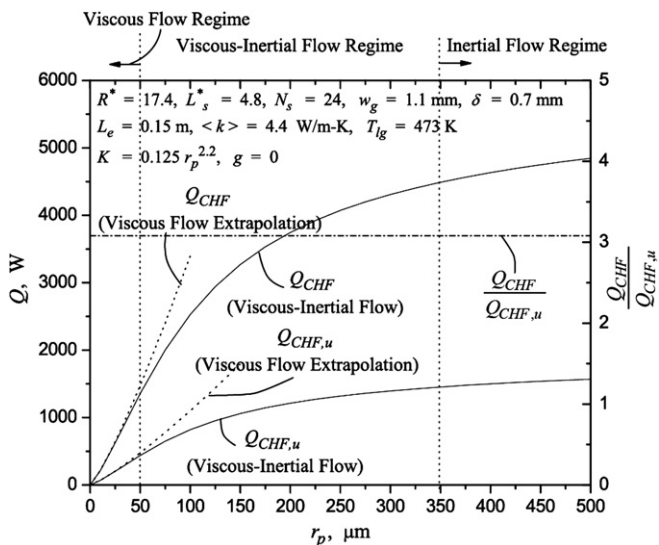


Fig. 10. Variation of the critical heat flow rate, with respect to the pore radius (influencing the permeability and the maximum capillary pressure) of the wick. The results for the modulated wick (prototype heat pipe) and the uniform wick, in the viscous- and inertial-flow regimes, are shown. The extrapolation of the critical heat flow rate in the viscous-flow-regime is compared with predictions in the viscous-inertial flow regime. Approximations of flow regimes (viscous-flow, viscous-inertial flow, and inertial flow regime) are also marked. The dimensionless critical heat flow rate  $Q_{CHF}/Q_{CHF,u}$  is also shown.

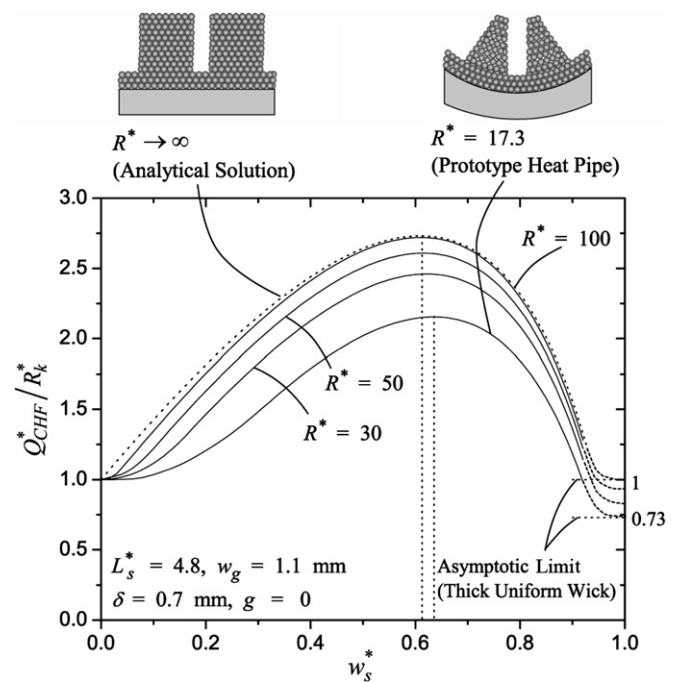


Fig. 12. Variation of the dimensionless figure of merit  $Q_{CHF}^*/R_k^*$  with respect to the dimensionless modulated wick pitch  $w_s^*$ , for increasing  $R^*$ . The asymptotic limits for the thin/thick, uniform wick heat pipes are also shown.

reaches a plateau where pore size (permeability) contribution counterbalances the inertial-flow pressure drop (this is called the inertial-flow regime). However, the 3.1 times enhancement of the critical heat flow rate, over the pore size range, is due to an increase in the cross-sectional area. This shows the liquid flow regime does not influence the enhancement. The closed-form solution developed in a viscous-flow regime (where the prototype heat pipe operates) predicts with good agreement (pore radius <math> < 50 \mu\text{m}</math>), while it shows discrepancy in the inertial-flow regime.

5.3. Modulated wick pitch,  $w_s^*$

The critical heat flow rate and the thermal resistance of a flat heat pipe ( $R^* \rightarrow \infty$ ) with variation of the  $w_s^*$  is shown in Fig. 11. The isothermal contour plot is also illustrated for  $w_s^* = 0.3$  and  $w_s^* = 0.9$ . The  $Q_{CHF}^* = 1$  in case of  $w_s^* \rightarrow 0$  due to the scarcity of modulated wick (stack) cross-sectional area, which is a thin, uniform wick. With  $L_s^* = 4.8$ , the unit enhancement linearly increases as the  $w_s^*$  increases, and finally it reaches 5.8 when it is a thick uniform wick ( $w_s^* = 1$ ). On the contrary,  $1/R_k^* \rightarrow 1$  as  $w_s^* \rightarrow 0$ , while it is 0.17 when  $w_s^* = 1$ . When  $w_s^* \rightarrow 0$ , the isothermal plot becomes nearly flat, which can be considered that the groove contributions are negligibly small, since infinite evaporation sites allow for the uniform thermal resistance across the wick. While  $w_s^*$  approaches 1, the isothermal contour lines also appear flat because the lack of evaporation sites provides a nearly uniform heat flow path up to the wick surface. The long path of the heat flow diminishes the heat pipe performance.

5.4. Pipe radius,  $R^*$

Fig. 12 shows the numerical results of  $Q_{CHF}^*/R_k^*$  with increasing  $R^*$ , and are compared with the analytical

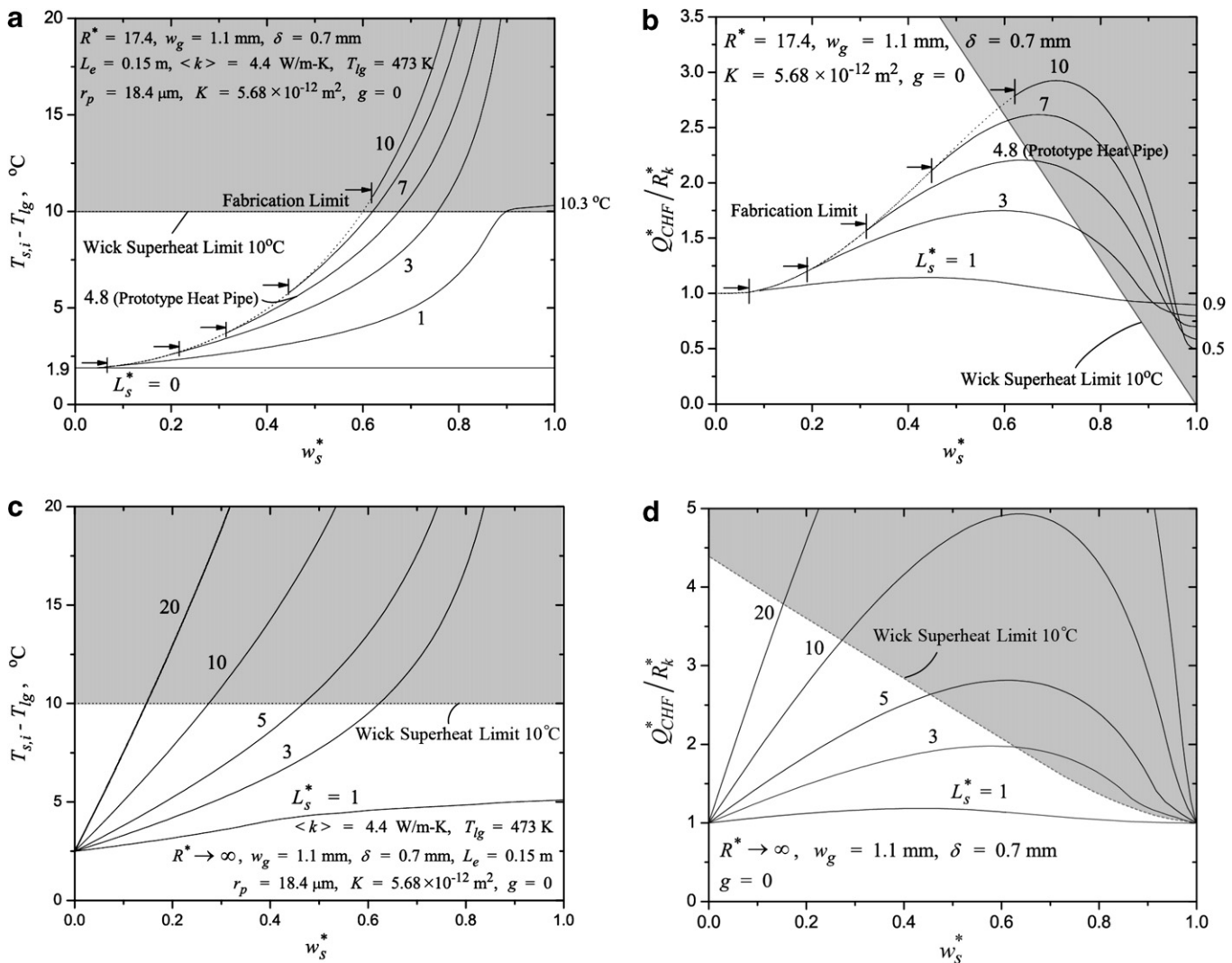


Fig. 13. Variation of the wick superheat and the dimensionless figure of merit  $Q_{CHF}^*/R_k^*$  with respect to the dimensionless modulated wick pitch  $w_s^*$  both in the circular (prototype) and the flat heat pipe. The wick superheat limit and the geometry constraints ( $L_{s,max}$ ) are also shown. (a) Wick superheat in the circular (prototype) heat pipe, (b) dimensionless figure of merit for the circular (prototype) heat pipe, (c) wick superheat in the flat heat pipe, and (d) dimensionless figure of merit for the flat heat pipe.

solution for the flat heat pipe ( $R^* \rightarrow \infty$ ). For a given  $R^*$ , the curve for  $Q_{CHF}^*/R_k^*$  is parabolic with a peak point representing the theoretically optimized wick structure. A very large  $R^*$  (keeping the height of stacks identical) provides the increased maximum  $Q_{CHF}^*/R_k^*$  since it allows for additional area of the capillary wick (tapered stacks becomes rectangular) which in turn results in reduction of the liquid flow resistance. The very large  $R^*$  also allows for the reduction of the optimal design of  $w_s^*$ . As  $w_s^*$  approaches 1, the modulated wick shows the same performance as the uniform wick since it is not able to provide sufficient contribution of the liquid supply to overcome the increased wick superheat. Also, the dimensionless heat pipe figure of merit is equal to 1 when  $w_s^*$  becomes 0 since the modulated wick eventually becomes a thin uniform wick as grooves are eliminated. Even though the radius of the heat pipe increases infinitely, the modulated wick heat pipe performance is limited by  $Q_{CHF}^*/R_k^* = 2.7$  (with  $L_s^* = 4.8$ ), which this is the best performance that the prototype heat pipe can operate. The optimal design of  $w_s^*$  decreases as the  $R^*$  increases, but the variation is negligibly small.

### 5.5. Stack height, $L_s^*$

As expected,  $L_s^*$  is one of the critical parameters controlling an axial viscous-drag liquid-flow resistance. A large  $L_s^*$  would be expected to allow for an increased liquid flow, which in turn results in a sufficient input heat flow rate. However, the improved heat flow rate brings considerable increase in wick superheat which results in nucleate boiling blocking the liquid circulation. Even though the enhancement of critical heat flow rate with the modulated wick could be theoretically enormous, the overall performance would be limited by the wick superheat limit. Fig. 13(a)–(d) illustrate the wick superheat and the computed values of  $Q_{CHF}^*/R_k^*$  for both the prototype (circular) heat pipe and the flat heat pipe. For the circular heat pipe, limited predictions are made due to a tapered stack structure at given geometry constraints: these conditions are plotted as dotted lines. Fig. 13(a) shows the wick superheat results with respect to  $w_s^*$  both for several values of  $L_s^*$  and 10 °C wick superheat limit for  $R^*$  of the prototype heat pipe. For  $L_s^* = 0$ , the wick superheat becomes 1.9 °C over all the range of  $w_s^*$  due to the lack of wick modulation, while wick superheat develops with an increase in  $w_s^*$ , when  $L_s^*$  is above zero. The higher  $L_s^*$  allows for larger wick superheat. To avoid a boiling problem, a selected operating zone (without shading) below wick superheat limit becomes an appropriate design domain for modulated wick heat pipes. For the prototype heat pipe, the design of  $L_s^* \geq 10$  is not appropriate since boiling problem would be expected. Fig. 13(b) shows the variation of  $Q_{CHF}^*/R_k^*$  for several values of  $L_s^*$ , and presents available operating zone bounded by the wick superheat limit. The modulated wick heat pipe shows improved performances as  $L_s^*$  increases. The  $L_s^* = 3$  shows lower performance compared to  $L_s^* = 4.8$ , the  $L_s^* = 7$  appears to be sensitive to fabrications around the

peak point. Considering the manufacturing uncertainty and the enhancement of the heat pipe, the optimal design for the stack height gives  $L_s^* \approx 5$ . For the flat heat pipe, Fig. 13(c) illustrates the variation of the predicted wick superheat with respect to  $w_s^*$  for several radius of  $L_s^*$ , and for  $R^* \rightarrow \infty$  showing 10 °C wick superheat limit. For  $L_s^* = 1$ , the variation of wick superheat becomes fairly small over all the range of  $w_s^*$  due to poor wick modulation, while the wick superheat dramatically increases with an increase of  $w_s^*$  when  $L_s^*$  becomes larger than 1. The flat heat pipe could have infinite height of stack because of no geometric constraint of pipe radius, but similarly, the modulated wick design should show an available operating region (without shading) below the wick superheat limit. In Fig. 13(d), the variation of  $Q_{CHF}^*/R_k^*$  for several values of  $L_s^*$  is given with respect to  $w_s^*$ , and presents an available

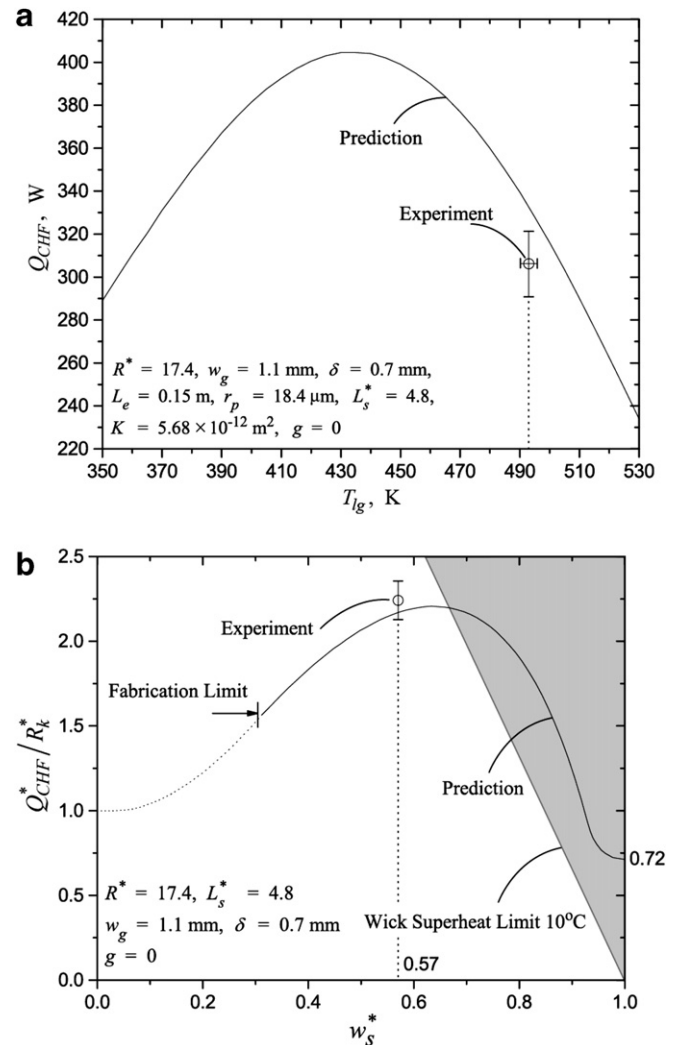


Fig. 14. The experimental result of the prototype heat pipe (in the horizontal placement) is compared with the prediction. (a) Comparison of the critical heat flow rate at operating temperature, and (b) comparison of the dimensionless figure of merit with respect to the dimensionless modulated wick pitch  $w_s^*$ .

operating zone bounded by the wick superheat limit. The modulated wick heat pipe shows improved performances as  $L_s^*$  increases, but the maximum enhancement, which is roughly  $Q_{CHF}^*/R_k^* = 4.5$ , is controlled by wick superheat limit. Considering the manufacturing uncertainty and the enhancement of the heat pipe, the optimal stack height becomes  $L_s^* = 5\text{--}10$ .

### 5.6. Comparison with experiment

In Fig. 14(a), the measured critical heat transfer rate (horizontal placement,  $g = 0$ ) is compared with the prediction (based on the developed models), with respect to the operating temperature. The predicted result over the range of  $T = 350\text{--}530$  K show a parabolic variation, with a peak around  $T = 435$  K. Note that for water as a working fluid, the combination of surface tension  $\sigma$ , liquid density  $\rho_l$ , viscosity  $\mu_l$ , heat of evaporation  $\Delta h_{lg}$ ,  $(\sigma\rho_l\Delta h_{lg}/\mu_l)$  also peaks around 435 K [7]. The predicted result (for the horizontal placement) overestimates the measurement with 5% uncertainty in the heat transfer rate and 1 °C in the operating temperature. These uncertainties are also shown in the figure.

Fig. 14(b) shows a comparison between the measurement (at the horizontal placement) and predictions, in terms of  $Q_{CHF}^*/R_k^*$  versus  $w_s^*$ . The approximated predictions using the geometry constants are plotted as a dotted line. Note that  $1/R_k^*$  is numerically estimated at a given geometry  $w_s^*$ . The  $Q_{CHF}^*/R_k^*$  shows asymptotic behavior for  $w_s^* = 0$  and  $w_s^* = 1$ . For  $w_s^* = 0$ ,  $Q_{CHF}^*/R_k^* = 1$ , since the modulated wick does not contribute to enhancement, while the modulated wick produces inferior performance ( $Q_{CHF}^*/R_k^* = 0.72$ ) appeared to the thick, uniform wick when  $w_s^* = 1$ . The experimental result is also shown,  $Q_{CHF}^*/R_k^* = 2.2$ .

## 6. Conclusion

The thermal-hydraulic dimensionless heat pipe figure of merit  $Q_{CHF}^*/R_k^*$  is successfully developed based on the proposed physical interpretations and network models in order to evaluate the enhancement of modulated wick heat pipes. In a viscous-flow regime ( $K \rightarrow 0$ ), the closed-form solution is developed for  $Q_{CHF}^*/R_k^*$ , while in an inertial-flow regime solutions are treated numerically due to necessity of iteration on the axial liquid pressure drop. Then  $Q_{CHF}^*/R_k^*$  is used to arrive at an optimal design of the modulated wick heat pipe, subject to an empirical wick superheat limit [9].

For the prototype heat pipe ( $R^* = 17.4$ , small permeability, titanium–water), the measured dimensionless heat pipe figure of merit  $Q_{CHF}^*/R_k^* = 2.2$  is in good agreement with the prediction (within 3%). The predicted  $Q_{CHF}^*/R_k^*$  also shows that the current modulated wick heat pipe is nearly optimized (using an empirical wick superheat limit of 10 °C [9]), despite manufacturing constraints.

A flat heat pipe is also considered (very large pipe radius) to eliminate tapering effect of the stacks, and the results then show the maximum enhancement in  $Q_{CHF}^*/R_k^*$

is 4.3 (all other aspects being the same as those of the prototype heat pipe). Similar results are found for the high permeability limit where the flow inertial and gravity forces play significant roles and the solution is obtained numerically.

## Acknowledgements

This work was sponsored by NASA Glenn Research Center under Contact NNC05TA36T with Duane Beach as the Technical Monitor. David Sarraf, Peter Dussinger, and Rod McClellan have helped with the heat pipe fabrication and testing, for which we are grateful.

## Appendix A. Two-dimensional conduction resistance of modulated wick

To determine  $\alpha$  in Eq. (21), the simulation work on the thermal resistance (related to wick superheat) is produced using Ansys 9.0. The unit cell for the computer simulation is presented in Fig. A.1. The unit cell contains half of stack and half of uniform wick, as well as adjacent pipe wall. The evaporation zone is postulated to be on the entire surface of modulated wick where the saturation temperature remains constant due to phase change. Thus, the saturation temperature at the evaporation zone is applied as the boundary condition, and the uniform heat flux is assumed at the outer surface of the pipe. An adiabatic condition is applied at the remaining surfaces due to expected symmetric geometry.

The temperature distributions within two different modulated wicks are shown in Fig. A.2(a) and (b). In these sim-

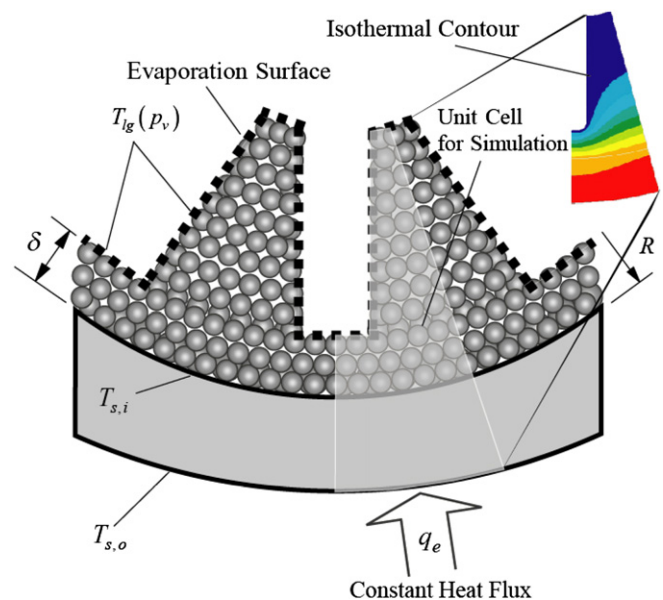


Fig. A.1. Key parameters and boundary conditions used in the two-dimensional conduction and thermal resistance analyses. The wick unit cell in the numerical simulations is also shown.

ulations, the wick stack pitches are  $N_s = 4$  and 12, the input heat is  $Q = 360$  W, and  $L_s = 4$  mm. For the small  $N_s$  (i.e.,  $N_s = 4$ ), the larger inner stack base allows for large heat input but longer conduction path, which in turn results in a higher thermal resistance. Conversely, for the large number of stack (i.e.,  $N_s = 12$ ), most of the heat flow is in the lower half of the stacks (due to large thermal resistance along the stack), but overall it leads to lower effective wick thermal resistance. The temperature distribution within the stack (from bottom to top) is illustrated in Fig. A.3. The 10 °C wick superheat limit is also shown. The wick superheat has a maximum value, 53.8 °C when  $N_s = 0$ . On the

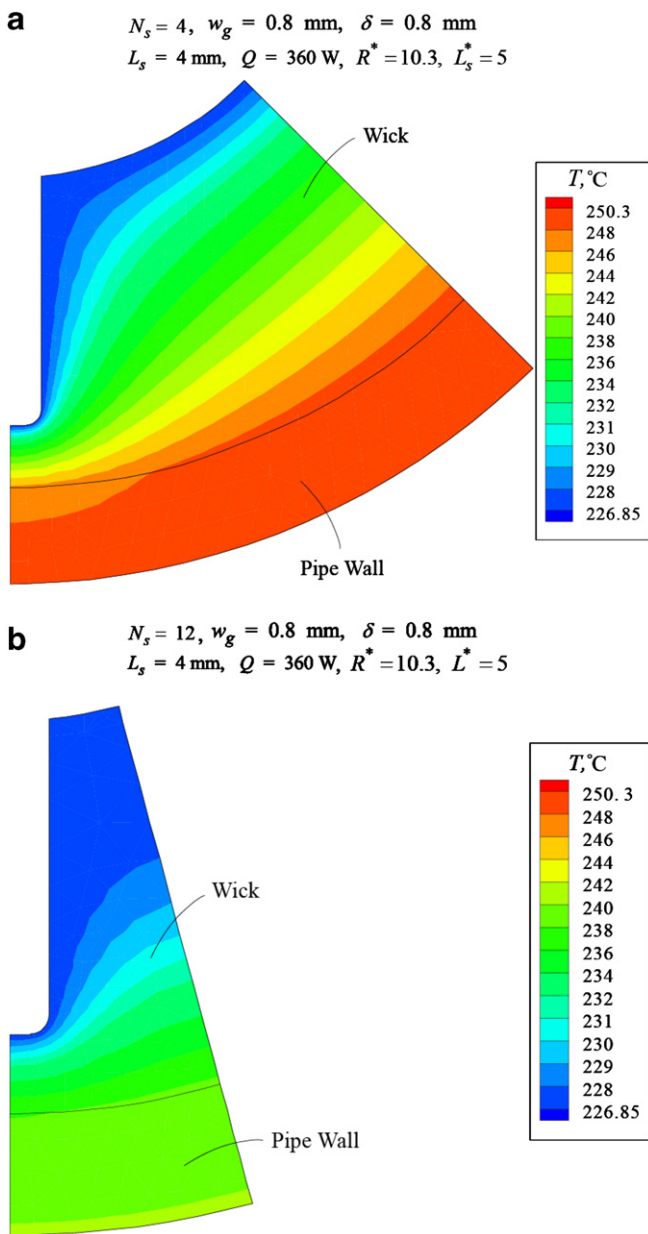


Fig. A.2. The predicted two-dimensional temperature distribution in the wick unit cell for  $Q = 360$  W with a constant temperature on the outer wall surface: (a)  $N_s = 4$ , and (b)  $N_s = 12$ .

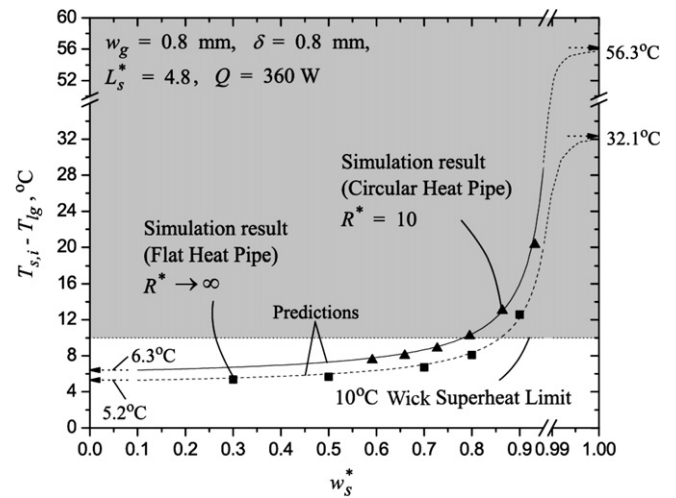


Fig. A.3. Variation of the wick superheat for the circular and flat heat pipes, with respect to the dimensionless modulated wick pitch  $w_s^*$ . The maximum (for thick, uniform wick) and minimum (for thin, uniform wick) wick superheats are also marked, as well as the empirical 10 °C wick superheat limit.

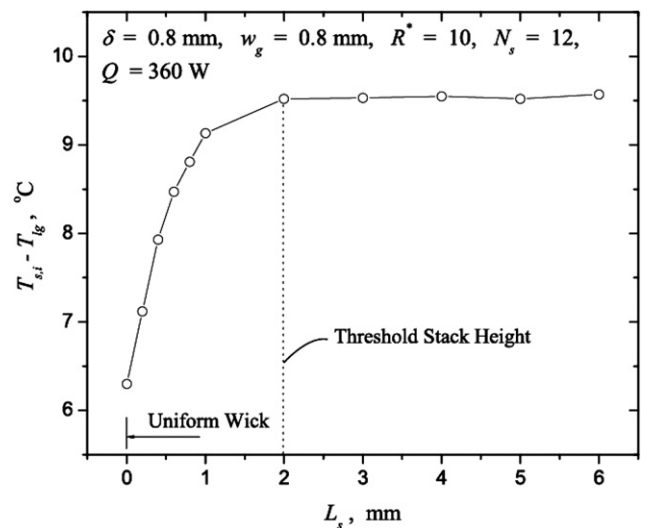


Fig. A.4. The computed variation of the wick superheat with respect to the stack height (used in the two-dimensional conduction and thermal resistance model). The threshold stack height is also shown.

other hand, the minimum wick superheat 6.3 °C is for the thin uniform wick ( $N_s \rightarrow \infty$ ).

Using Eqs. (20) and (21), the wick superheat and the thermal resistance are given as

$$\Delta T_w = \frac{Q \ln \left( 1 - R^{*-1} - \alpha \frac{w_g w_s^*}{1 - w_s^*} \right)^{-1}}{2\pi L_e \langle k \rangle}, \quad \text{and}$$

$$R_k = \frac{\Delta T_w}{Q} = \frac{\ln \left( 1 - R^{*-1} - \alpha \frac{w_g w_s^*}{1 - w_s^*} \right)^{-1}}{2\pi L_e \langle k \rangle}. \quad (\text{A.1})$$

The equation is also extended to the flat heat pipe as below,

$$\Delta T_w = \frac{Q \left( 1 + \alpha \frac{w_g w_s^*}{1 - w_s^*} \right)}{A_f \langle k \rangle}. \quad (\text{A.2})$$

The value  $\alpha = 0.15$  is determined from the numerical simulation results with 2.2% (cylindrical heat pipe) and 3.9% (flat heat pipe) RMS errors.

A study of the stack height effect on the wick superheat is also done in case of  $N_s = 12$ . Fig. A.4 shows that the wick superheat is almost independent on the height of the stack, if its height is greater than a threshold value (in this example,  $L_s = 2$  mm). For  $L_s$  is larger than the threshold value, the results of Fig. A.3 show that  $\delta'$  is only a function of  $w_s^*$ .

## References

- [1] J.H. Rosenfeld, J.E. Lindemuth, Heat transfer in sintered groove heat pipes, in: Proceedings of the International Heat Pipe Conference, Tokyo, Japan, 1999.
- [2] W.G. Anderson, D. Sarraf, P.M. Dussinger, Development of a high temperature water heat pipe radiator, in: Proceedings of the International Energy Conversion Engineering Conference (IECEC), San Francisco, 2005, ISBN 1563477696.
- [3] W.G. Anderson, R. Bonner, J. Hartenstine, J. Barth, High temperature titanium–water heat pipe radiator, Space Technology & Applications International Forum (STAIF) Conference, vol. 813, American Institute of Physics, New York, 2006, pp. 91–99.
- [4] M. Kaviany, Principles of Heat Transfer in Porous Media, second ed., Springer, New York, 1999.
- [5] M. Kaviany, Principles of Heat Transfer, Wiley, New York, 2002.
- [6] S.G. Liter, M. Kaviany, Pool-boiling CHF enhancement by modulated porous-layer coating: theory and experiment, Int. J. Heat Mass Transfer 44 (2001) 4287–4311.
- [7] A. Devarakonda, W.G. Anderson, Thermophysical properties of intermediate temperature heat pipe fluids, Space Technology & Applications International Forum (STAIF) Conference, vol. 746, American Institute of Physics, New York, 2005, pp. 79–186.
- [8] A. Faghri, Heat pipe Science and Technology, Taylor & Francis, New York, 1995.
- [9] G.S. Hwang, M. Kaviany, Critical heat flux in thin, uniform particle coatings, Int. J. Heat Mass Transfer 49 (2006) 844–849.
- [10] S.W. Chi, Heat Pipe Theory and Practice, McGraw-Hill, New York, 1976.
- [11] G.P. Peterson, An Introduction to Heat Pipes: Modeling, Testing, and Applications, Wiley, New York, 1994.